Synchrotron X-ray Data Processing and Visualization Techniques for Analysis of Functional Materials

A Thesis Presented

by

Charles Clark

to

The Graduate School

in Partial Fulfillment of the

Requirements

for the Degree of

Master of Science

in

Materials Science and Engineering

Stony Brook University

May 2023

Stony Brook University

The Graduate School

Charles Clark

We, the thesis committee for the above candidate for the

Master of Science degree, hereby recommend

acceptance of this thesis.

Yu-chen Karen Chen-Wiegart – Thesis Advisor
Assistant Professor, Department of Materials Science & Chemical Engineering,
Stony Brook University

Gary Halada – Second Reader
Associate Professor, Department of Materials Science & Chemical Engineering,
Stony Brook University

Denis Leshchev – Third Reader
Assistant Physicist, ISS Beamline, NSLS-II,
Brookhaven National Laboratory

This thesis is accepted by the Graduate School

Celia Marshik
Interim Dean of the Graduate School

Abstract of the Thesis

Synchrotron X-ray Data Processing and Visualization Techniques for Analysis of Functional Materials

by

Charles Clark

Master of Science

in

Materials Science and Engineering

Stony Brook University

2023

The objective of this thesis work is to demonstrate the application of both standard and specialized data science and visualization tools to synchrotron X-ray data analysis. Each chapter highlights an application of such tools to a different study of functional materials, including: in-situ X-ray absorption spectroscopy (XAS) of phase evolution at an MnO_2 electrode during battery cycling, a kinetic study of molten salt dealloying (MSD) using 3D X-ray nanotomography, and grazing-incidence wide angle X-ray scattering (GIWAXS) analysis of phase evolution during solid-state interfacial dealloying (SSID) in a Ti-Cu/Mg alloy system. In each case core Python data science packages such as NumPy, Matplotlib, and Pandas were used to efficiently carry out routine data analysis tasks such as data organization and visualization. Subsequently, a range of more advanced tools were employed, ranging from more specialized Python packages such as SciPy, PeakUtils, or pyMCR, to entire analysis applications like Avizo for 3D data analysis, or Materials Project's XAS database.

Overall, the wide range of tools available, coupled with the effectiveness of data science packages, highlights the increasing critical need for researchers in synchrotron science to possess a solid understanding of data science tools. This need is further amplified by the substantial percentage of multimodal experiments conducted at synchrotron facilities, including but not limited to Brookhaven National Laboratory's National Synchrotron Light Source II (NSLS-II) where the experiments detailed in this thesis took place. As synchrotron science continues to generate increasingly complex, multidimensional datasets, the need for efficient data processing and visualization tools becomes even more crucial. Additionally, continued efforts to better integrate these tools with experimental beamlines will be crucial for enabling researchers to seamlessly handle and analyze complex datasets.

Table of Contents

List of Figures

List of Tables

List of Abbreviations

XAS	X-ray Absorption Spectroscopy
MSD	Molten Salt Dealloying
GIWAXS	Grazing-Incidence Wide Angle X-ray Scattering
SSID	Solid-State Interfacial Dealloying
NSLS-II	National Synchrotron Light Source II
MCR	Multivariate Curve Resolution
ALS	Alternating Least Squares
LCF	Linear Combination Fitting
LOF	Lack of Fit
PCA	Principal Component Analysis
SVD	Singular Value Decomposition
EFA	Evolving Factor Analysis
SIMPLISMA	Simple-to-use Interactive Self-modelling Mixture Analysis
ISS	Inner Shell Spectroscopy
MSE	Mean Squared Error
GUI	Graphical User Interface
SEM	Scanning Electron Microscopy
XRD	X-ray Diffraction
XANES	X-ray Absorption Near Edge Structure
PC	Principal Component
FXI	Full Field X-ray Imaging
SSMD	Solid-State Metal Dealloying
CMS	Complex Materials Scattering
FWHM	Full-Width Half-Max
ROI	Region of Interest

Acknowledgments

First, I want to thank my advisor Dr. Yu-chen Karen Chen-Wiegart. Her continued advice and support were instrumental in completing this work. She has always inspired me through her hard work and dedication to science, and her compassion and empathy for students is truly unmatched. I am very grateful to have had the opportunity to work under her guidance.

Second, I would like to thank Dr. Gary Halada. As director of Stony Brook's Engineering Science program Dr. Halada's work had a great impact on my undergraduate education. Moreover, his enthusiasm and love for science means that working with him is always a pleasure. I also appreciate him taking the time to review this thesis and share his expertise in materials science.

Third, I would like to thank Dr. Eli Stavitski and Dr. Denis Leshchev of NSLS-II's ISS beamline. Discussions with them have been eye-opening in new ways to think about X-ray spectroscopy, particularly using the language of linear algebra. Their support has also facilitated my growth as both a synchrotron scientist and a data scientist. I would also like to thank Dr. Leshchev for reviewing this thesis. His input on the MCR discussion in Chapter 1 was especially valuable and led to several interesting discussions.

I would also like to thank Dr. Nav Nidhi Rajput. I first learned the foundations of scientific programming in Python form Dr. Rajput. It is because of her teaching that I had the necessary base to do the analysis work presented here.

Moreover, I would like to acknowledge the kindness and support from other members of the Chen-Wiegart group, including Dr. Chonghang Zhao, Dr. Xiaoyang Liu, Arthur Ronne, Cheng-Chu Chung, Nicole Zmich, Varun Kankanallu, Xioayin Zheng, Dean Yen, and Karol Dyro. With special thanks to Varun Kankanallu, Xiaoyang Liu, Chonghang Zhao, and Cheng-Chu Chung for allowing me to work on their projects and then use that work in this thesis.

Finally, I would like to acknowledge my family for their love, encouragement, and support from the very beginning.

Financial Acknowledgements

This research used resources and the Inner-Shell Spectroscopy Beamline (ISS, 8-ID) of the National Synchrotron Light Source II, a U.S. Department of Energy (DOE) Office of Science User Facility operated for the DOE Office of Science by Brookhaven National Laboratory under Contract No. DE-SC0012704.

This research used resources of the Center for Functional Nanomaterials (CFN), which is a U.S. Department of Energy Office of Science User Facility, at Brookhaven National Laboratory under Contract No. DE-SC0012704.

This work was supported as part of the Center for Mesoscale Transport Properties (m2M/t), an Energy Frontier Research Center funded by the U.S. Department of Energy, Office of Science, Basic Energy Sciences, under Award # DE-SC0012673.

This material is based on work supported by the National Science Foundation under Grant No. DMR-1752839.

This work was supported as part of the Molten Salts in Extreme Environments (MSEE) Energy Frontier Research Center, funded by the U.S. Department of Energy, Office of Science, Basic Energy Sciences. BNL, and ORNL are operated under DOE contracts DE-SC0012704, and DE-AC05-00OR22725, respectively.

Chapter 1. Multivariate Curve Resolution Applied to X-ray Absorption Spectroscopy*

1.1 Introduction

1.1.1 XAS Datasets

X-ray absorption spectroscopy (XAS) is a powerful technique for analyzing chemical state and local structure of a wide range of materials in different applications [1-3]. During an XAS experiment the absorption coefficient $\mu(E)$ of a sample is measured as a function of an incident X-ray beam energy around a target elemental energy edge (usually denoted E_0). The acquired spectrum is based on the electronic and structural state of the selected element in the sample for elemental and chemical sensitive analysis. XAS experiments produce complex datasets as each spectrum typically consists of several hundred data points, and an entire series of spectra can be collected that evolve as a function of parameters such as time, space, chemical composition, *etc*. Researchers are generally interested in the changes in spectra due to variations in the experimental parameter under study, therefore it is also helpful to regard each spectrum as a single multiparameter data point within the broader scope of experimental analysis.

Before any analysis can be done on a set of XAS spectra they must be normalized to remove the effects of measurement conditions on the data, such as sample preparation, sample thickness, detector settings, *etc*. The normalization procedure shifts and scales an XAS spectrum such that

* Part of the chapter related to battery analysis is based on a manuscript published in Energy & Environmental Science: Varun R. Kankanallu, Xiaoyin Zheng, Denis Leschev, Nicole Zmich, Charles Clark, Cheng-Hung Lin, Hui Zhong, Sanjit Ghose, Andrew M. Kiss, Dmytro Nykypanchuk, Eli Stavitski, Esther S. Takeuchi, Amy C. Marschilok, Kenneth J. Takeuchi, Jianming Bai, Mingyuan Ge and Yu-chen Karen Chen-Wiegart, *Elucidating a dissolution–deposition reaction mechanism by multimodal synchrotron X-ray characterization in aqueous Zn/MnO2 batteries.* Energy & Environmental Science, 2023.

the pre-edge region of the normalized spectrum is at $\mu = 0$, and the characteristic post-edge features oscillate around the value $\mu = 1$ [4].

Since XAS requires an X-ray source with finely tunable incident energy and high photon flux to achieve sufficient data quality, the technique is most often performed at synchrotron radiation facilities [2]. Although laboratory based methods are core to the history of XAS, and in recent years have attracted significant interest [5]. In the case that multiple chemical states of the selected element are present in the sample then each chemical state may be treated as a "pure" component, and as a consequence of Beer's Law, the total acquired spectrum is equal to a linear combination of the "pure" component spectra weighted by each component's relative concentration in the sample [2], *i.e.*:

$$\mu(E) = \sum_{i=1}^{N} c_i s_i + \varepsilon \tag{1.1}$$

In this equation N represents the number of pure components in the sample, c_i and s_i are the respective concentration and spectrum of the i^{th} pure component, and ε represents experimental noise in the measurement.

From here equation (1.1) can be extended to consider an entire XAS dataset (*e.g.*, from a time or space resolved experiment) as the multiplication of a concentration matrix C with a spectral matrix S:

$$D = CS^T + \varepsilon \tag{1.2}$$

Here D represents a dataset composed of m measurements each with n energy points, thus having dimensions $\dim(D) = (m \times n)$. The rows of C represent the concentrations of each N pure

component across the m measurements, thus dim(C) = ($m \times N$), and the rows of S are the reference spectra of the N pure components, thus dim(S) = ($n \times N$). Here, ε has been extended to a data matrix with dim(ε) = ($m \times n$) which still represents experimental noise in the dataset.* Figure 1.1 shows a schematic of the matrix multiplication for further illustration. Now that the XAS dataset is expressed in a matrix form the tools of linear algebra can be applied for a more rigorous mathematical analysis of experimental results.

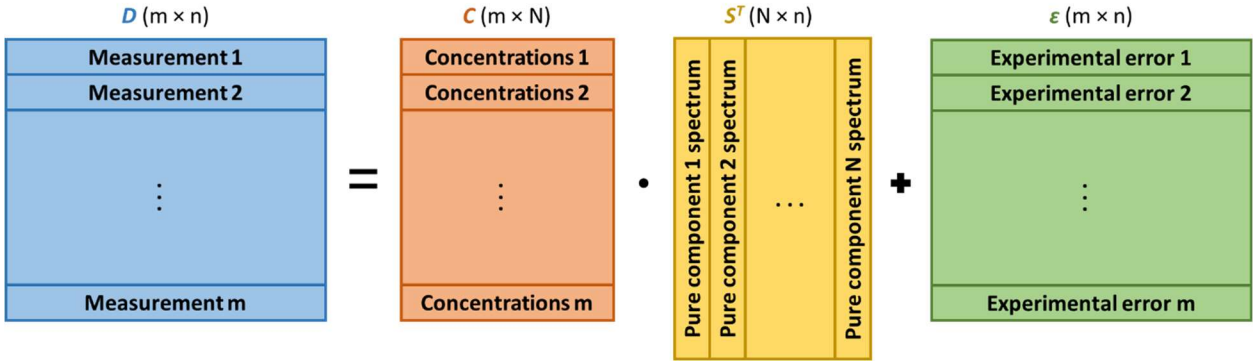

Figure 1.1 Schematic of equation (1.2) to express XAS dataset (D) as matrix multiplication of a concentration matrix (C) and matrix of pure component spectra (S) plus a residual error matrix (ε).

1.1.2 Multivariate Curve Resolution – Alternating Least Squares (MCR-ALS)

Generally, the goal of any XAS data analysis is to determine the pure components in a sample and their respective concentrations from an experimental dataset. In terms of equation (1.2) this means determining the concentration profile matrix C and pure component spectra matrix S, for a given dataset matrix D. In some cases, the spectra of the pure components making up a sample are

* Note that several different but equivalent notations exist in the literature for expression of spectral datasets in matrix form. Here the notation from [6] is adopted. See references [2, 7] for example uses of other notations and further details.

already known (*i.e.*, the *S* matrix is already determined) based on prior knowledge of the chemical reactions or sample fabrication processes, and only the concentration profiles need to be fitted to the experimental data. A very common choice for XAS analysis in such a situation is linear combination fitting (LCF). LCF essentially applies least squared fitting to fit concentration profiles to the XAS dataset based on the provided pure component spectra.

Multivariate curve resolution (MCR) refers to a suite of techniques used to decompose spectral datasets when neither the pure component spectra nor concentration profiles are known. Alternating least squares (ALS) is becoming a popular MCR method due to its relative simplicity in implementation as well as robustness [2]. MCR-ALS starts with an initial guess of the concentration profiles or pure component spectra, and then iteratively applies least squares regression to first fit whichever matrix was not provided (*e.g.*, fitting C_1 if an initial guess S_0 was given), then uses the result of this fitting to re-fit the matrix for which an initial guess was provided (*e.g.*, using C_1 to fit a new estimation of the pure component spectra S_1). This alternating fitting process is repeated until a breaking condition is met. The breaking condition may be the convergence or divergence of the fitting based on the change to a defined lack-of-fit (LOF) parameter, or simply that a user-defined maximum number of iterations has been reached. Figure 1.2 shows a schematic representation of the MCR-ALS fitting algorithm.

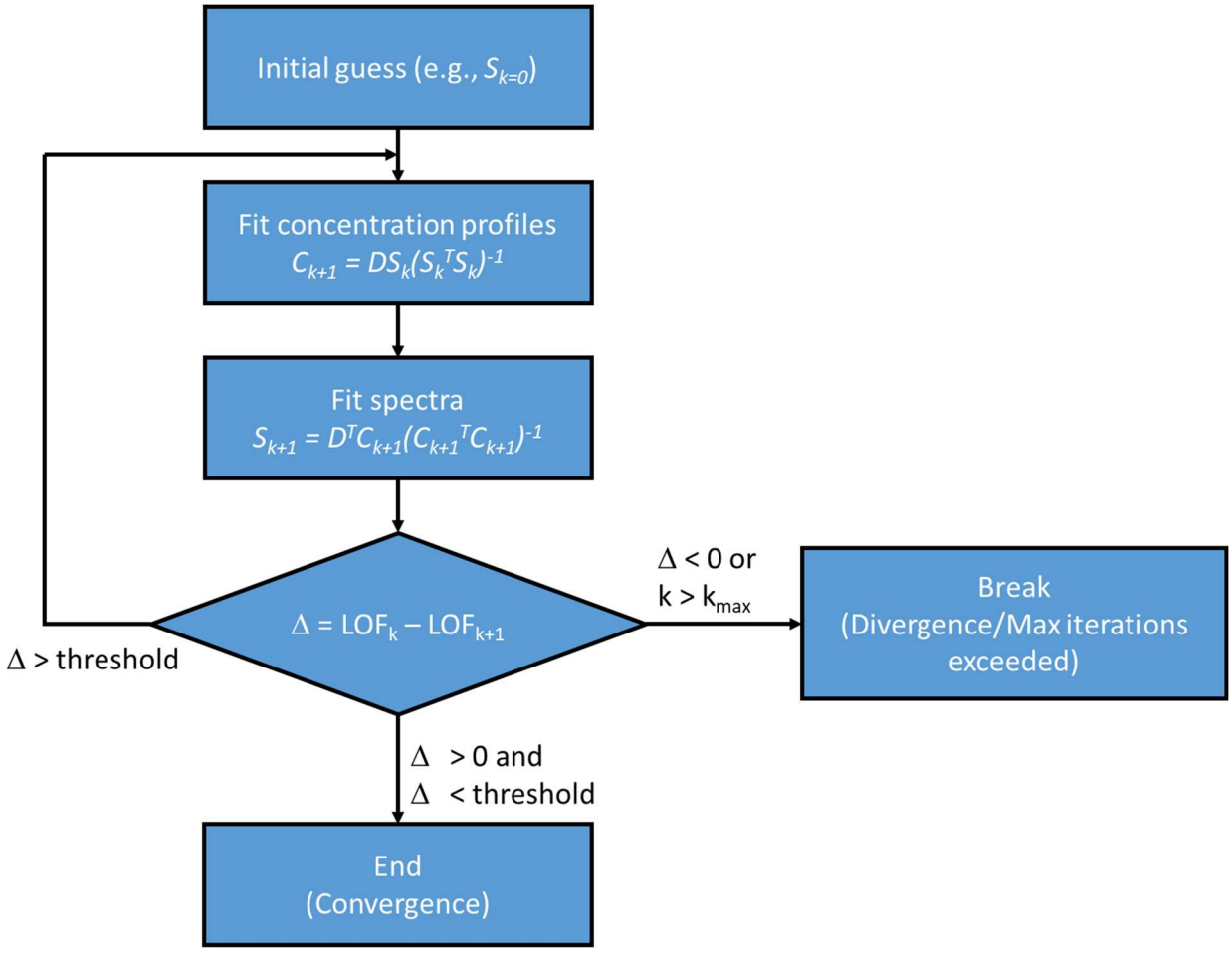

Figure 1.2 Flowchart diagram of typical MCR-ALS algorithm. Note that a more positive Δ indicates a better fitting result, while a more negative Δ indicates a worse fitting result.

Several constraints may also be applied during the ALS fitting to ensure physical validity of the fitted results [2]. For instance, a sum-to-one (also sometimes called normalization) constraint is usually applied to the concentration profiles to ensure mass balance is satisfied (i.e., $\sum_{i=1}^{N} c_i = 1$ for all m measurements). Likewise, non-negativity constraints are usually applied to both the concentration profiles and pure component spectra since there is no valid physical interpretation of a negative concentration or negative absorption coefficient.

In an ideal case MCR-ALS would reveal the exact chemical composition of a selected element in a sample throughout an experiment. However, in practice many factors impact the result of any MCR-ALS fitting including data quality, normalization of spectra, and perhaps most importantly the initial guess of spectra or concentration profiles provided. Therefore, any MCR-ALS analysis requires careful consideration of several parameters and an informed interpretation of the resulting fit.

Another important consideration in the analysis of MCR-ALS fitting results is the so-called rotational ambiguity. Rotational ambiguity refers to the fact that the solution produced by an MCR-ALS fitting routine is in general not unique and exists within a space of feasible solutions that satisfy the convergence criteria. Applying constraints to the MCR-ALS fitting process, such as the aforementioned sum-to-one and non-negativity constraints, help to reduce rotational ambiguity by restricting the size of the unique solution space. The best way to estimate the degree of uncertainty due to rotational ambiguity is still being investigated, however software such as MCR-Bands is openly available which implements one approach for quantitatively estimating the degree of rotational ambiguity [8].

1.1.3 Generating an Initial Guess

The first step in applying MCR to an experimental dataset is an estimation of the number of pure components present in the data. Mathematically this corresponds to an estimation of the rank of the dataset matrix *D*. This estimation can be achieved via principal component analysis (PCA) of the dataset, which is often performed through singular value decomposition (SVD) of the *D* matrix. SVD decomposes *D* into the following form:

$$D = U\Sigma V^T \tag{1.3}$$

In this form U is an ($m \times m$) and V is an ($n \times n$) matrix, each with columns that can be respectively thought of as the eigen-concentration profiles and eigen-spectra composing the D dataset. The columns of V may also be referred to as the "principal components" of D. Σ is then an ($m \times n$) diagonal rectangular matrix whose elements are the singular values of D. The singular values are arranged in descending order along the diagonal of Σ, and in essence rank the importance of the columns of U and V in describing the dataset. In actuality the columns of U and V have no physical interpretation, but instead if the first r columns of U and V are considered with the first r rows of Σ, then their multiplication in the form of equation (1.3) is the best least-squares approximation of D using r components [7]. Thus, based on the SVD of D a critical value for r can be determined for which the key features of the dataset are described without describing the experimental noise. This critical value represents the number of pure components found in the dataset and there are several quantitative methods for its determination [2].

Once the number of pure components has been determined there are several ways to generate an initial guess for the pure component spectra (S_0) or concentration profiles (C_0). More advanced mathematical techniques include evolving factor analysis (EFA) or the simple-to-use interactive self-modelling mixture analysis (SIMPLISMA) algorithms [2]. However, a simpler approach of choosing the correct number of reference spectra measured on material standards can also be utilized to create an initial guess for S_0.

1.2 Implementation and Example Application

1.2.1 MCR-ALS Implementation in Python

XView is a python-based XAS data analysis software package developed by Eli Stavitski and Denis Leshchev of NSLS-II's Inner Shell Spectroscopy (ISS, 8-ID) beamline [9]. XView makes use of the pyMCR package developed by NIST which implements alternating regression scheme MCR algorithms in python, including MCR-ALS [6]. The pyMCR package allows users to perform MCR fitting by first creating a specially defined class which includes the regression algorithm to be used and any fitting constraints, then a simple function call can fit an initial guess of either pure component spectra or concentration profiles to a dataset. Constraints that can be used include the aforementioned sum-to-one and non-negativity constraints, as well as fixing any elements of the initial guess so that they are not varied during the fitting process, among others. Fitted results are returned as easily accessible NumPy arrays. pyMCR currently uses the mean-squared error (MSE) as its LOF parameter, which is calculated via the following:

$$MSE = \frac{\sum_{i=1}^{m}\sum_{j=1}^{n}\left(D_{i,j} - D_{i,j}^{calc}\right)^2}{m \times n} \tag{1.4}$$

While XView remains as a software under constant development, a great amount of functionality has been developed on top of the pyMCR package. For example, within XView users can perform SVD and PCA on a dataset to determine the number of pure components, something which is not implemented in pyMCR. XView also implements a graphical user interface (GUI) which allows for more user-friendly creation of datasets, initial guesses, and fitting parameters. Results of any MCR projects in XView are then stored as json files that can be accessed later for further analysis and manipulation.

1.2.2 Application to Battery Materials

Using XView, MCR-ALS was applied to an in-situ experimental dataset studying the material phase evolution at an MnO_2 electrode in (2M $ZnSO_4$ + 0.1M $MnSO_4$) electrolyte during battery cycling. From scanning electron microscopy (SEM), X-ray diffraction (XRD) and X-ray nanotomography analysis it was clear that new Zn-Mn complex phases were forming in the electrodes as they undergo cycling; however, the exact chemical nature of these phases was uncertain. Thus, MCR analysis, combined with SVD/PCA, was applied to the X-ray absorption near edge structure (XANES) region of XAS data around the Mn K-edge to gain better insight into the number of phases formed during the experiment and the chemistry of these phases.

Figure 1.4 shows plots from the SVD/PCA conducted in XView. From this analysis it was concluded that there were likely three, though possibly four, pure component phases present in the data. This conclusion was based on several aspects of the SVD/PCA. First, as seen in Figure 1.4a the fourth principal component (PC) is less smooth than the first three, implying that this component begins to describe the experimental noise in the dataset rather than important spectral features [7]. Second, in Figure 1.4b the scree plot, which essentially plots the importance of each PC by its singular value and chi-square value [2], begins to level off around four PC's. Finally, the autocorrelation of the fourth eigen-concentration profile is significantly lower than the first three. Autocorrelation is a measurement of the degree to which changes in a value are correlated with previous changes. This is a valuable metric for XAS PCA since no drastic changes are expected in any spectral features from one measurement to another. Therefore, a low autocorrelation for the concentration profile of a XAS PC can indicate that the PC is mostly describing noise in the dataset.

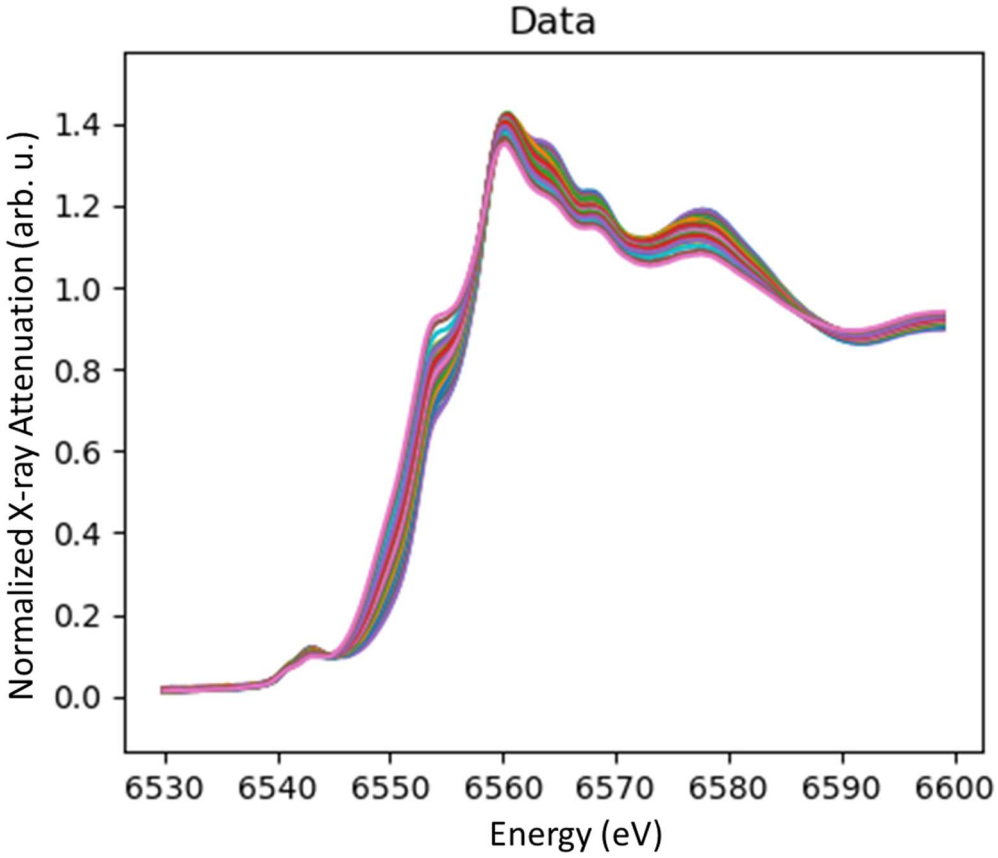

Figure 1.3 Mn K-edge XAS dataset from in-situ MnO_2 electrode experiment loaded into XView and cropped to XANES region.

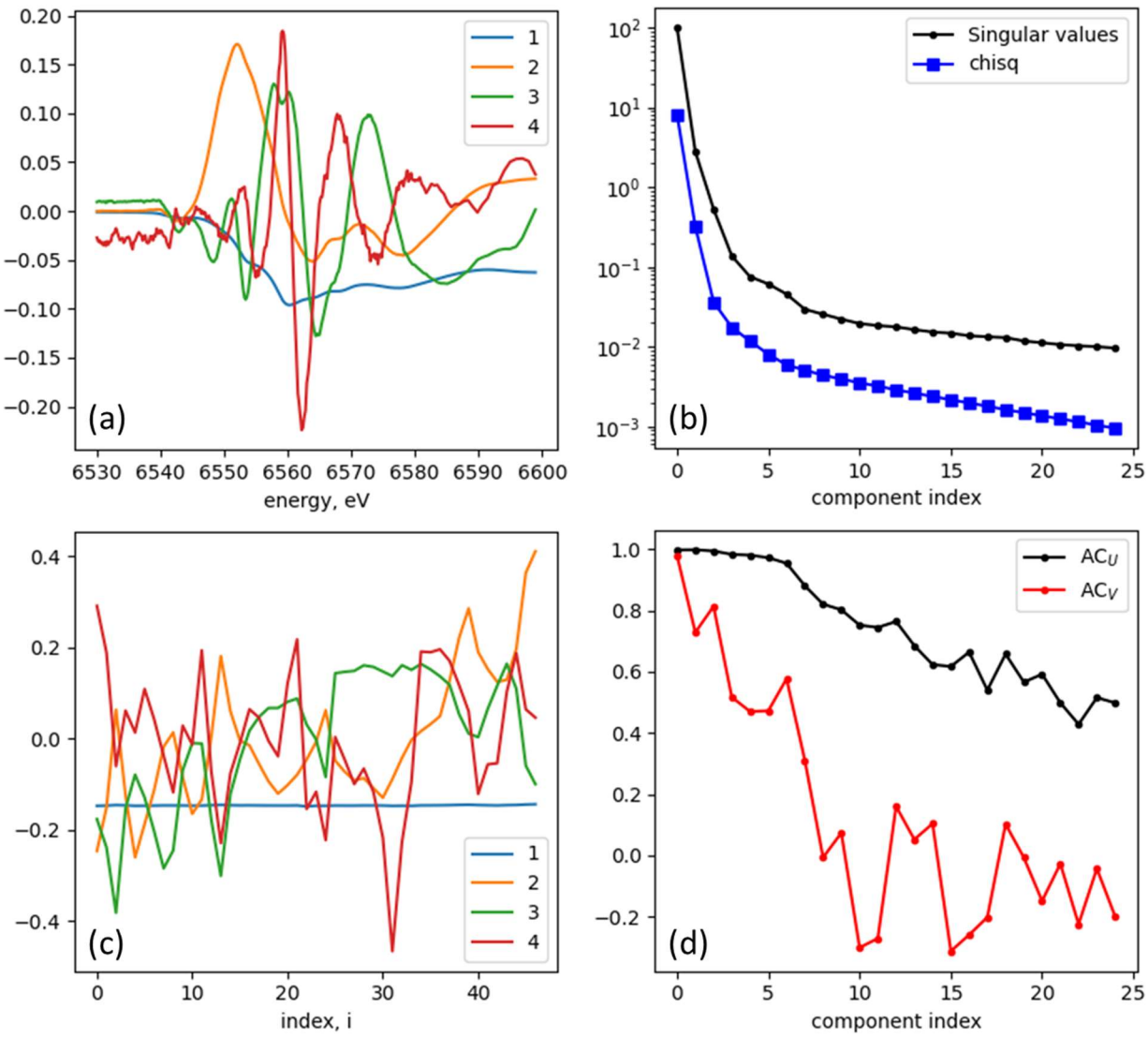

Figure 1.4 SVD/PCA of MnO_2 electrode in-situ experimental dataset: (a) plot of first four eigen-spectra/PC's, (b) scree plot for varying number of PC's, (c) first four eigen-concentration profiles, and (d) autocorrelation for eigen-spectra (black) and eigen-concentration profiles (red).

Based on the PCA of the dataset several potential MCR models were created and tested for the experimental data. The MCR models used included reference spectra from MnO_2 and $MnSO_4$ standards, as well as reference spectra from a Zn-Mn complex electrodeposited on carbon black, and spectra acquired on MnO_2 electrodes that had been further cycled for ex-situ experiments (see

Table 1.1). For each model we applied the standard non-negativity and sum-to-one constraints, and then selected a combination of reference spectra that had been measured on material standards for initial guesses. The fitting results for each model were then plotted and evaluated based on how well the fit compared to the real dataset as well as the physical validity of the refined spectra and concentration profiles.

Table 1.1 MCR models tested on MnO_2 in-situ experimental dataset. ED1 represents a spectrum acquired on Zn-Mn complex electrodeposited on carbon black believed to resemble a Zn-Mn complex formed during battery cycling. 8C, 16C, and 32C Charge indicate spectra acquired on further cycled MnO2 electrodes during ex-situ experiments.

Model #	*MnO_2*	*$MnSO_4$*	*ED1*	*8C Charge*	*16C Charge*	*32C Charge*
1	Fix	Fix	Vary			
2	Fix	Fix		Vary		
3	Fix	Fix			Vary	
4	Fix	Fix				Vary
5	Fix	Vary	Vary			
6	Fix	Vary		Vary		
7	Fix	Vary			Vary	
8	Fix	Vary				Vary
9	Fix		Vary	Vary		
10	Fix		Vary		Vary	
11	Fix		Vary			Vary
12	Vary					Vary
13	Vary				Vary	
14	Vary		Vary			Fix
15	Vary	Vary	Vary			Vary
16	Fix	Fix	Vary			Fix

Based on these criteria Model 10, shown in Figure 1.5 was determined to give the best result. This model's initial guess consisted of a reference MnO_2 spectrum which was fixed during the fitting process, as well as two other references which were believed to be close to the Zn-Mn complex phases that form during the battery cycling and were allowed to vary. Fixing the MnO_2 spectrum also helps to reduce the rotational ambiguity for the fitting results of this model since it effectively

adds another constraint to the fitting process. The fitted concentration profiles show the relative concentration of MnO_2 gradually decreases throughout the experiment, as expected, while one of the potential Zn-Mn complexes gradually increases. The spectrum for this gradually increasing phase has also been qualitatively noted to be rather similar to a calculated $ZnMn_2O_4$ XAS spectrum from The Materials Project [10-12]. Moreover, sharp short-term increases and decreases in MnO_2 concentration correspond to the battery cycling between discharge and charge, as indicated by blue and red dashed lines on the fitted concentration profile plot. The other potential Zn-Mn complex also fluctuates with the battery discharge and charge, which could indicate a reversibly forming complex phase. However, this phase's relative concentration stays roughly constant throughout the experiment, including the very start before any Zn-Mn complexes are expected to have formed. Therefore, further refinement of the model will likely be needed to understand exactly what this fitted spectrum represents physically.

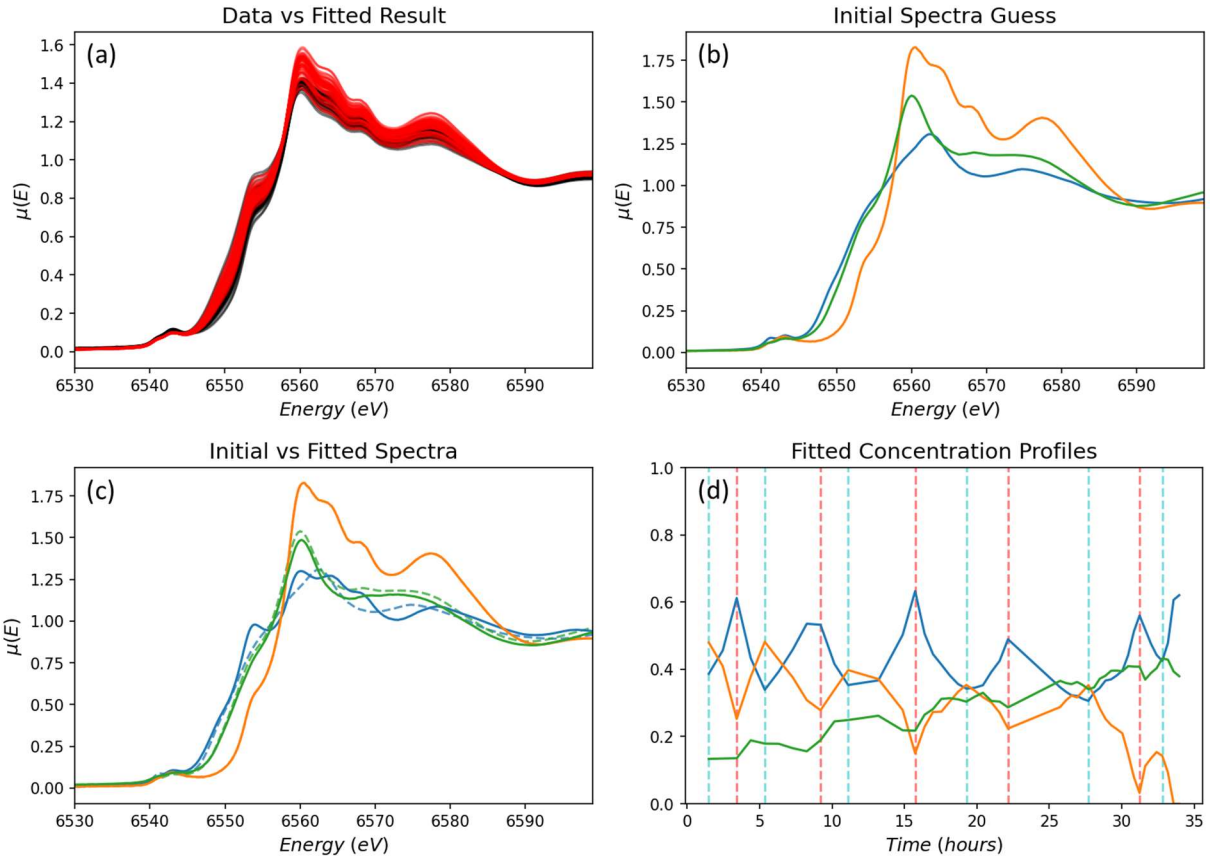

Figure 1.5 MCR-ALS model applied to MnO_2 electrode experiment dataset determined best based on quality of fit as well as physical interpretation of results: (a) experimental dataset (black) compared to MCR fit results (red), (b) spectra guess consisting of MnO_2 reference spectrum (orange) and two other references believed to resemble Zn-Mn complexes formed during the experiment (blue, green), (c) refined spectra after fitting (solid) compared to initial spectra guesses (dashed), note that MnO_2 reference was fixed to not vary during fitting, and (d) corresponding fitted concentration profiles with dashed vertical lines indicating battery cycling between discharge (cyan) and charge (red).

1.2.3 Future Work

While the selected model applied to the MnO_2 experimental data shows promising results, further analysis and model refinement will be needed to fully describe the XAS data. To start, the remaining refined reference spectrum (blue in Figure 1.5) requires further comparison to known XANES spectra to determine the chemistry it represents. Our initial hypothesis was that the

spectrum could represent a combination of a formed Zn-Mn complex phase and signal from the electrolyte solution based on qualitatively analysis of the spectrum's core features. However, so far attempts to resolve in the spectrum in such a way (*e.g.*, Models 15 and 16 in Table 1.1) have been unsuccessful. Thus, further testing and analysis is required. For instance, XANES modeling on the MCR results obtained may provide a significantly different physical interpretation of the currently undetermined spectrum. Moreover, MCR modeling can also be performed on the Zn K-edge data from the same in-situ experiment. This would be very valuable because any Zn-Mn complex phases should be represented in the refined spectra of the MCR results for both datasets, allowing for cross-validation of these phases. Furthermore, as XView is continuously developed new features such as EFA or SIMPLISMA algorithms may be implemented which would provide new methods for generating initial MCR guesses that could provide unique perspectives on the dataset. In addition, implementing algorithms such as MCR-Bands would allow future analysis to better estimate rotational ambiguity in any fitted results. Finally, further application of MCR to other types of datasets and systems will help to develop our understanding of the technique including its capabilities and limitations.

Chapter 2. Multi-dimensional Data Visualization and Quantification Techniques Applied to Nanotomography Datasets*

2.1 Introduction

Molten salt dealloying (MSD) is a promising technique for fabrication of micro/nanoporous metallic materials, which have a wide range of potential applications due to their high specific surface area, low density, and other desirable properties [13, 14]. Studying MSD was originally motivated by the salt-induced corrosion of engineering materials in the design of next generation nuclear and solar power plants [15-18]. Thus, by understanding the kinetic evolution of alloy materials during the MSD process, both the fabrication of micro/nanoporous materials and prevention of corrosion attacks in future concentrated solar and nuclear power plant designs can be advanced. Synchrotron X-ray nano-tomography is a powerful way to study the three-dimensional (3D) morphological and chemical evolution of materials during processes such as MSD due to the high spatial resolution and fast data acquisition times which allow for high quality real-time observations of the dealloying process during in-situ experiments. For instance, the Full Field X-ray Imaging beamline of NSLS-II is capable of acquiring a full 3D tomography scan in one minute with 30 nm resolution [19]. Such experiments generate very large multi-dimensional datasets. Therefore, there is a need to apply advanced data visualization and quantification techniques to such datasets to understand the kinetics of MSD.

* Part of the chapter is based on a manuscript in preparation: Xiaoyang Liu, Kaustubh K. Bawane, Charles Clark, Michael E. Woods, Phillip Halstenberg, Xianghui Xiao, Wah-Keat Lee, Lu Ma, Steven Ehrlich, Sheng Dai, Katsuyo Thornton, Mingyuan Ge, Ruchi Gakhar, Lingfeng He, Yu-chen Karen Chen-Wiegart *Elucidating the Transition of 3D Morphological Evolution of Binary Alloys in Molten Salts with Metal Ion Additives*.

2.2 Three-dimensional Data Visualization

Two in-situ tomography experimental datasets were acquired at the Full Field X-ray Imaging (FXI, 18-ID) beamline of NSLS-II to observe MSD of Ni-20Cr alloy micro-wire in KCl-$MgCl_2$ molten salt mixtures with 1 wt.% $EuCl_3$ additive. For the first experiment a 50-50 molar ratio of KCl-$MgCl_2$ was used, while the second experiment used a eutectic (68-32 molar ratio) mixture of KCl-$MgCl_2$. In both cases the samples were heated to 700 °C for the duration of the experiment. The details of the sample preparation and experimental procedure for the *in situ* synchrotron X-ray nano-tomography studies can be found in prior publications [13, 20].

Commercial data visualization and analysis software Avizo (Thermo Fisher Scientific, v. 9.3.0) was used to create 2D pseudo cross-sectional views and 3D volume renderings of the experimental datasets to observe pore formation and evolution during the MSD process. Within Avizo selected scans from the datasets were first cropped to smaller regions of interest near the edge of the Ni-20Cr wire to better observe pore evolution. Then a 3D median filter was applied to the data with a range of 18 pixels to reduce noise for better visualization. Distinct colormaps were also applied to the 3D volume renderings of each dataset to better aid visualization. The final data visualizations were placed in time series, as shown in Figure 2.1, to display pore evolution over time and differences in pore growth for the two salt mixtures.

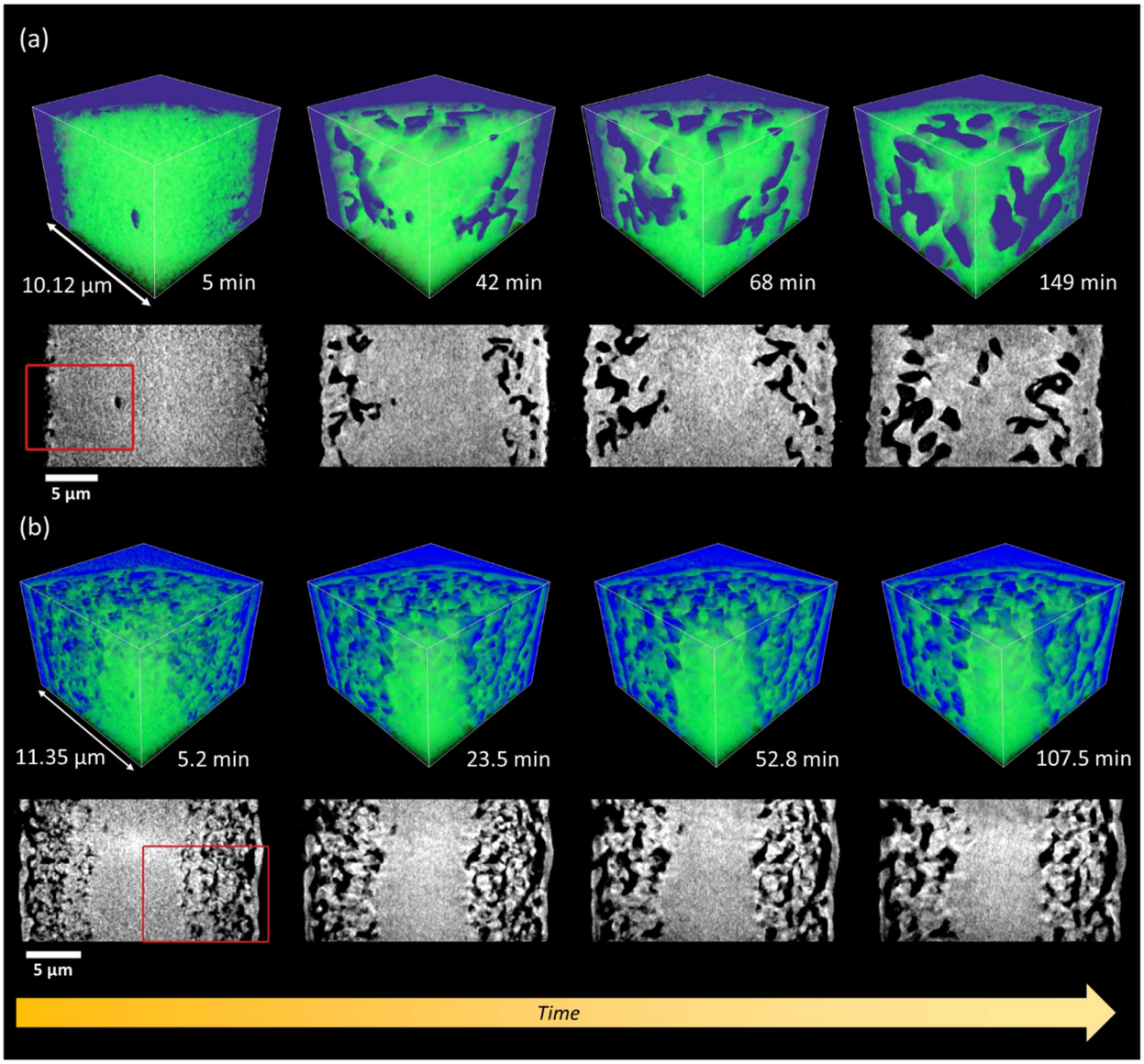

Figure 2.1 Data visualization of pore evolution in Ni-20Cr microwire during MSD in KCl-$MgCl_2$ molten salt mixture with 1 wt. % $EuCl_3$ additive. Regions of interest used for 3D volume rendering are indicated with red boxes on 2D pseudo cross-sections. (a) Dealloying in 50-50 molar ratio KCl-$MgCl_2$ mixture. (b) Dealloying in eutectic KCl-$MgCl_2$ mixture.

2.3 Image Segmentation and Morphological Quantification

To perform quantitative analysis on the in-situ datasets, the data was first cropped to remove unnecessary background and overly noisy data measured far from the center of the images with

very low signal-to-noise ratio due to low photon counts. Image cross correlation was then used to align the whole tomography time series via volume registration on the cropped data. Python code developed in-house at the FXI beamline of NSLS-II was used to perform the cross correlation via fast Fourier transforms of the 3D volumes [21]. Segmentation was then performed on the 3D images to distinguish between the alloy material, and the rest of the image (i.e., molten salt mixture and pores within the micro-wire). For the 50-50 KCl-$MgCl_2$ dataset a 3D Gaussian filter with standard deviation equal to 3 pixels was applied before doing segmentation to suppress noise. For this dataset segmentation was done by first determining a threshold from the X-ray attenuation histogram of the middle slice of each 3D image. The histograms were primarily bimodal, so the threshold can be determined automatically. The thresholding was conducted through an in-house Python script which utilizes SciPy's *find_peaks* function on the negative of the image histogram (i.e., the image histogram mirrored over the x-axis). The largest peak on the negative histogram corresponds to the deepest valley on the original histogram, which separates the two modes of the distribution. Therefore, the value at the largest negative peak can be used for the image threshold. For each image, pixels with X-ray attenuations above the threshold were marked as alloy material, while those with attenuations below the threshold were marked as the molten salt mixture or pores (see Figure 2.2(a)).

A similar process was applied to perform segmentation on the eutectic KCl-$MgCl_2$ dataset. First a 3D Gaussian filter with standard deviation equal to 2 pixels was applied. The filter size was reduced due to smaller features being removed by a larger filter size. Again, the attenuation histogram of the middle slice of each 3D image was used for thresholding. However, due to increased complexity of the histograms the *threshold_minimum* function from scikit-image package in Python was used to determine the threshold for each image, rather than the previously

used in-house method (see Figure 2.2(b)). This function returns a threshold based on the minimum method, which continually smooths the histogram until there are only two maxima, at which point the minimum between them is determined to be the threshold [22].

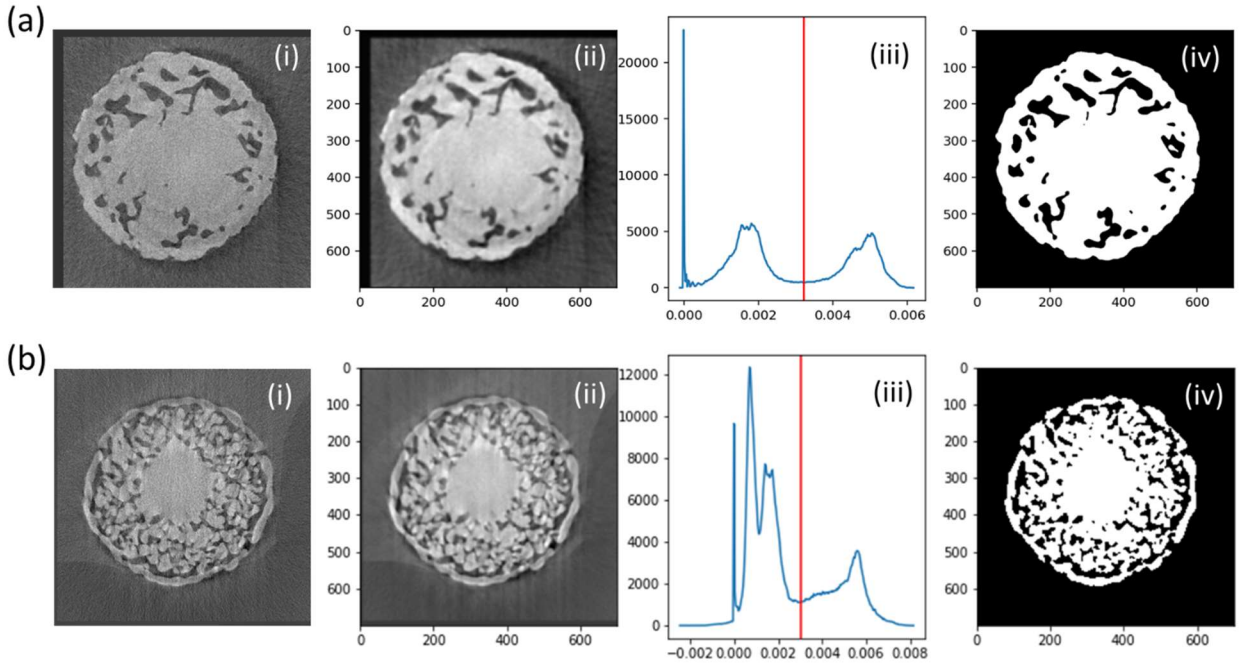

Figure 2.2 Demonstration of segmentation process on example scans from MSD of Ni-20Cr microwires: (a) in 50-50 molar ratio KCl-$MgCl_2$ and (b) in eutectic KCl-$MgCl_2$ mixture. (i) a middle pseudo cross-section image of scan after cropping and alignment, (ii) the middle pseudo cross-section image after applying 3D Gaussian filtering, (iii) filtered image histograms with threshold values marked in red, (iv) final binarized image after segmentation. Note the increased complexity in the histogram for (b) compared to (a).

With the segmentation process, the datasets were converted into series of binary images for quantitative analysis. Volume loss was calculated by counting the number of pixels marked as the Ni-20Cr alloy material for each image and normalizing by the initial amount of alloy material in each dataset. This gave the fraction of initial volume remaining as a percentage for each scan. It is

important to note that artifacts in the image segmentation occasionally resulted in the volume loss analysis showing greater than 100% of the starting material for some scans.

To perform porosity calculations further data processing was required. Specifically, a mask around the sample needed to be created so that the pores inside the sample could be distinguished from the molten salt mixture outside the sample. To create such a mask the convex hull of the 2D images in each binarized 3D image stack was computed using the *convexHull* function in OpenCV [23]. Since the samples resemble a mostly convex, almost circular shape in the 2D cross-sections, the convex hull provided a good approximation of the sample edges. Therefore, the non-material pixels inside the convex hull mask could be marked as pores while those outside the convex hull mask could be marked as the molten salt mixture. Now each scan is a ternary image consisting of three distinct phases: pixels marked as the alloy material, the pores in the micro-wire, and the outer molten salt mixture as shown in Figure 2.3. The porosity of each scan was then calculated by taking the fraction of pixels within the convex hull mask that are marked as pores.

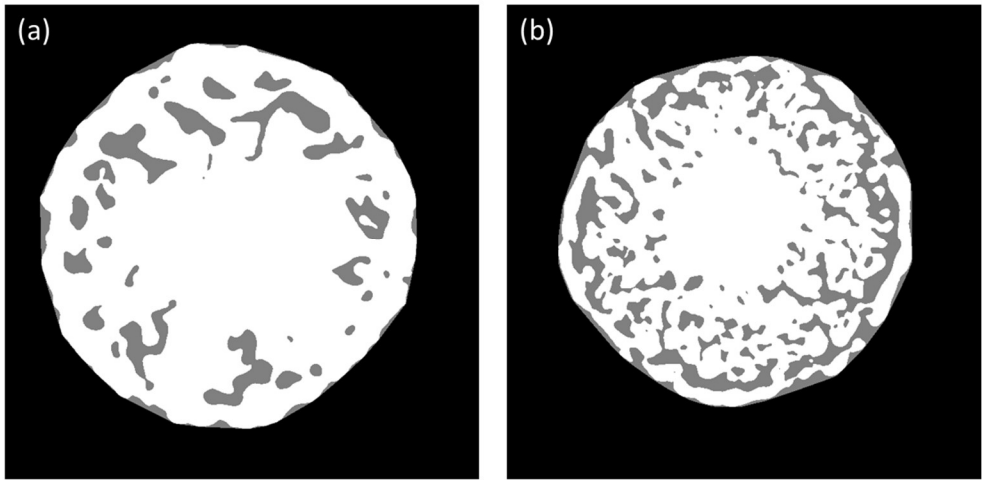

Figure 2.3 Convex hull masking applied to example scans from 50-50 molar ratio KCl-$MgCl_2$ (a) and eutectic KCl-$MgCl_2$ (b) datasets. Pixels marked as molten salt mixture are black, while those marked pores are grey, and those marked as alloy material are white.

2.4 Results and Discussion on Volume Loss and Porosity Evolution

The final calculated volume losses and porosity measurements were plotted across the experimental duration for both datasets, as seen in Figure 2.4. Overall, the reaction kinetics for the eutectic mixture was much faster than that of the 50-50 molar ratio KCl-$MgCl_2$. Volume loss occurred more quickly during MSD in eutectic KCl-$MgCl_2$ and the final percentage of volume remaining was also lower (~90% compared to ~94%). In each experiment an initial rapid increase of porosity was observed, but porosity growth slowed as dealloying continued. However, in the eutectic KCl-$MgCl_2$ mixture the initial porosity growth was much more rapid, the porosity leveled off much faster, and the final porosity was higher relative to dealloying in the 50-50 KCl-$MgCl_2$ (~27% compared to ~22%).

Since grain boundaries serve as a shortcut for reactions and diffusion, the differences in morphological evolution could be explained by competition along grain boundaries between surface diffusion of the more noble element (Ni) and dissolution of the less noble element (Cr) [16]. For instance, if the surface diffusion of Ni occurs much faster than Cr dissolution, then Ni atoms could aggregate and passivate the surface of the grains, significantly slowing volume loss and pore growth. Inversely, if Cr dissolution occurs faster than Ni surface diffusion, significantly faster reactions may occur. With this understanding it is possible that the different composition KCl-$MgCl_2$ molten salt mixtures caused changes in the relative kinetics of the Ni surface diffusion and the Cr dissolution along grain boundaries. In either case these experiments directly show that the composition of molten salt can on its own affect the MSD corrosion process. Future work may establish a more quantitative relationship between the ratio of KCl to $MgCl_2$ in molten salt and corrosion of Ni-Cr alloys.

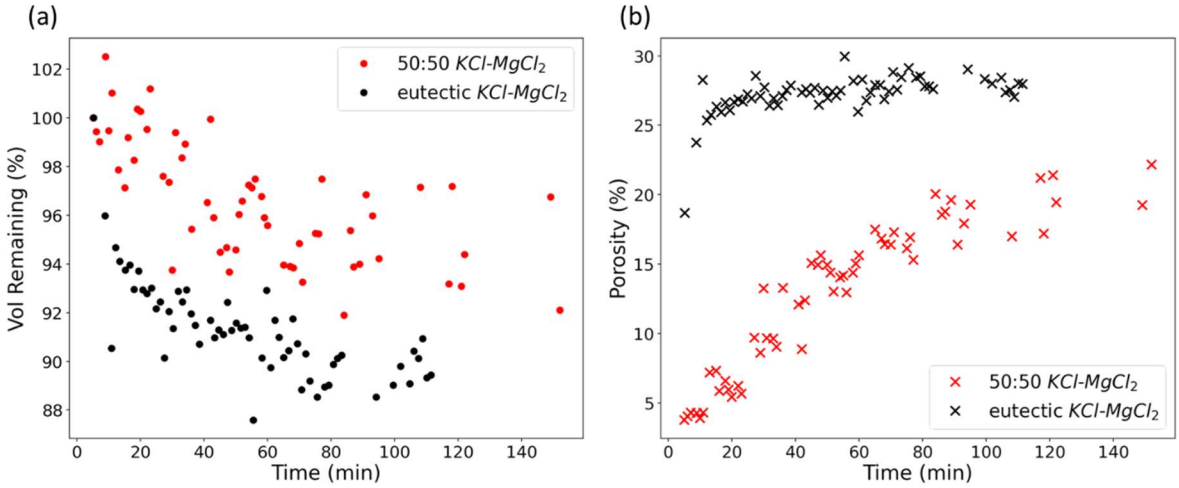

Figure 2.4 Comparison of volume loss (a) and porosity growth (b) for MSD in the 50-50 molar ratio KCl-$MgCl_2$ (red) and eutectic KCl-$MgCl_2$ (black). Note that artifacts in the segmentation process produced some volumes above 100% for the 50-50 dataset.

Chapter 3. Multiparameter Analysis of GIWAXS Data for Thin-Film Solid State Interfacial Dealloying*

3.1 Introduction

Thin-film solid state interfacial dealloying (SSID), also called thin film solid state metal dealloying (SSMD), is another emerging technique for fabrication of nanoporous materials. Specifically, SSID is a subset of metal-agent dealloying. During metal-agent dealloying a metal is used as a solvent to selectively dissolve one or more components from an alloy, causing the remaining components to self-reorganize into a metal-metal nanocomposite or nanoporous structure. Applying SSID to a thin film geometry has been recently demonstrated, and makes use of shorter dealloying times to fabricate finer features than dealloying bulk materials, as well as opening the possibility to combine SSID with various substrates for functional applications [24]. However, the material design criteria including the underlying thermodynamics and kinetics processes for thin film SSID systems are not yet fully understood. Traditionally the mixing enthalpies of the metal solvent with the elements in the starting alloy would be compared to determine the thermodynamic favorability of dealloying, but this has been shown to be insufficient in describing SSID systems [25]. Thus, there is a need to explore the multiparameter space which characterizes a SSID system in order to first understand the evolution and kinetics of that particular system, then apply this understanding in guiding exploration of future systems.

* Part of the chapter is based on data associated with a manuscript published in Acta Materialia: Chonghang Zhao, Lin-Chieh Yu, Kim Kisslinger, Charles Clark, Cheng-Chu Chung, Ruipeng Li, Masafumi Fukuto, Ming Lu, Jianming Bai, Xiaoyang Liu, Hui Zhong, Mingzhao Liu, Sanjit Ghose, Yu-chen Karen Chen-Wiegart, *Kinetics and Evolution of Solid-State Metal Dealloying in Thin Films with Multimodal Analysis.* Acta Materialia, 2022: p. 118433

3.2 Exploration of Parent Alloy Composition and Dealloying Time

Grazing-Incidence Wide-Angle X-ray Scattering (GIWAXS) data was acquired at the Complex Materials Scattering (CMS, 11-BM) beamline, NSLS-II, as part of a systematic study of a thin film SSID system consisting of a Ti-Cu parent alloy film with a Mg solvent film deposited on top of the parent alloy. The acquired GIWAXS spectra were compared to reference peak locations using commercial phase identification software (Jade 9, Materials Data, Inc.) to determine the metallic and intermetallic phases present in the thin films at various stages of the dealloying process. Several processing parameters were varied including parent alloy composition, dealloying time, and dealloying temperature. Moreover, for GIWAXS analysis the incident angle of the X-ray beam can be varied, with a larger incident angle probing deeper regions of the thin film samples.

In order to visualize the multiparameter space that characterizes the Ti-Cu/Mg system several waterfall plots were created using Matplotlib and other Python tools. Before any plotting a fitted quadratic background was subtracted from each GIWAXS pattern using the PeakUtils package in Python [26]. These plots show how the GIWAXS patterns evolves as single parameter is varied, allowing for specific aspects of the dealloying kinetics to be understood. For example, Figure 3.1 shows a waterfall plot for varying Ti-Cu parent alloy compositions after dealloying at 460 °C for 30 minutes with an incident angle of 0.3°, except for the 50-50 sample for which 15 minute dealloying time is shown due to the 30 minute sample breaking. In Figure 3.1 a selected portion of the GIWAXS patterns is shown to highlight the presence of peaks for $CuMg_2$ and Cu_2Mg phases indicated with green and blue arrows respectively. Previous analysis of this dealloying system had shown a phase transformation from $CuMg_2$ to Cu_2Mg during the course of the dealloying process

at 460°C [24]. From Figure 3.1 it can be seen that for initial concentrations of 10 and 20 at.% Ti (i.e., 90 and 80 at.% Cu) this transformation proceeded to completion since only Cu_2Mg peaks are present, but for higher Ti concentrations and thus lower Cu concentrations the kinetics were slower so both $CuMg_2$ and Cu_2Mg peaks can be seen to some degree; with the exception of 90 at.% Ti for which neither Cu-Mg intermetallic phases can be seen.

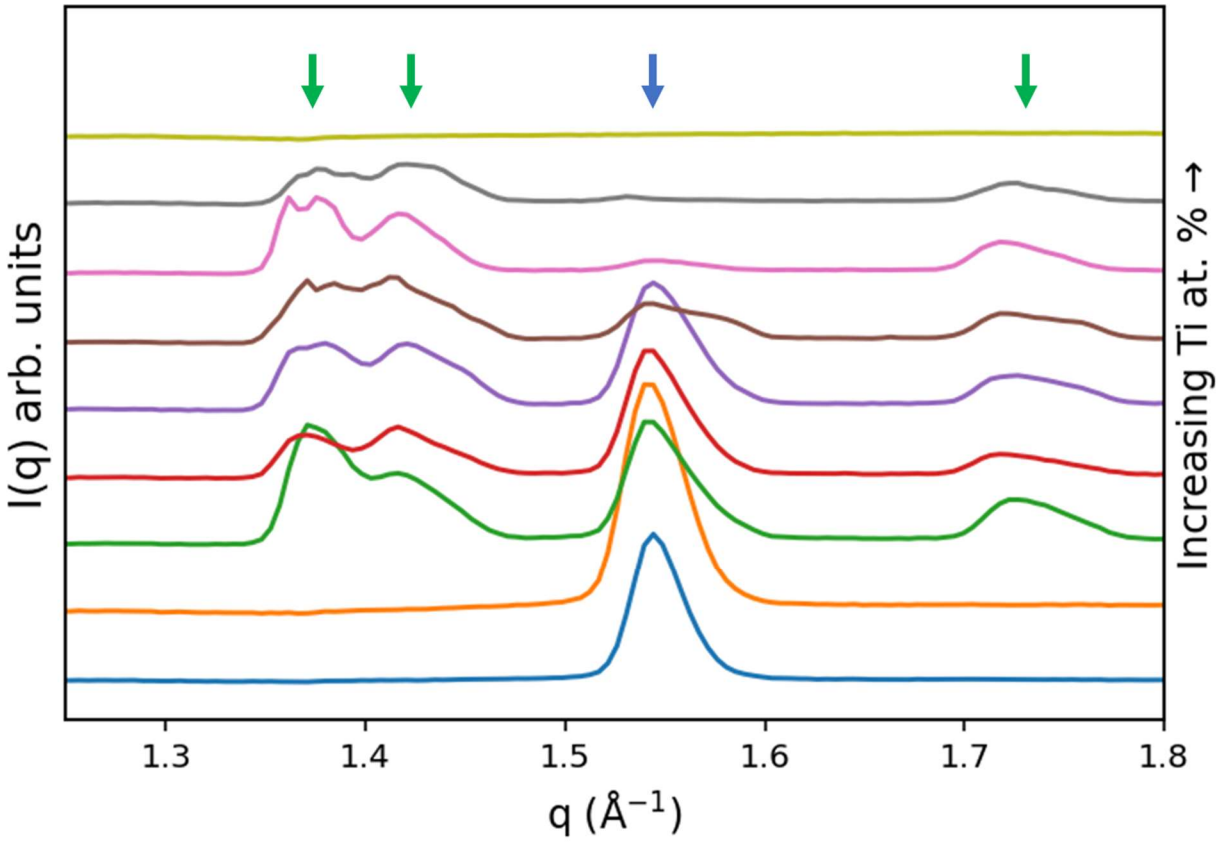

Figure 3.1 GIWAXS patterns of samples dealloyed at 460 °C for 30 minutes with varying Ti-Cu parent alloy composition shown in the q range between ~1.25 and 1.8 $Å^{-1}$. Compositions varied from 10 at.% Ti (blue) to 90 at.% Ti (yellow) with 10 at.% increment. Note that for 50 at.% Ti (purple) a dealloying time of 15 minutes is shown due to the 30 minute sample breaking. Arrows show approximate locations of reference peaks for $CuMg_2$ (green) and Cu_2Mg (blue) phases.

Furthermore, the spectra acquired at varying dealloying times was analyzed in a similar way. For this experiment only two parent alloy compositions (Ti-Cu 10-90 and 30-70) were measured after dealloying at 460° C for both 7.5 and 30 minutes. The spectra acquired at an incident angle of 0.3° for the 30-70 samples are shown in Figure 3.2 to highlight peak shoulders in the 7.5 minute GIWAXS pattern at roughly 2.82 $Å^{-1}$ and 2.98 $Å^{-1}$. These shoulders may correspond to the presence of a TiCu intermetallic phase which was identified to have diffraction peaks at those approximate locations. This observation helped in addressing a concern that no TiCu intermetallic phases were previously identified in the spectra, since some TiCu intermetallics would likely form in the parent alloy before the Cu has been selectively removed. Since these shoulders are only present for the sample dealloyed for 7.5 minutes, but not for 30 minutes, it is possible this intermetallic phase formed early in the dealloying process and was later transformed as the Cu leached into the Mg film. While this is only initial evidence for such an intermetallic phase, further experiments could verify the presence of this phase by testing samples with even shorter dealloying times, or by comparing the spectra of the 30-70 sample dealloyed for 7.5 minutes after chemical etching of the Mg top layer.

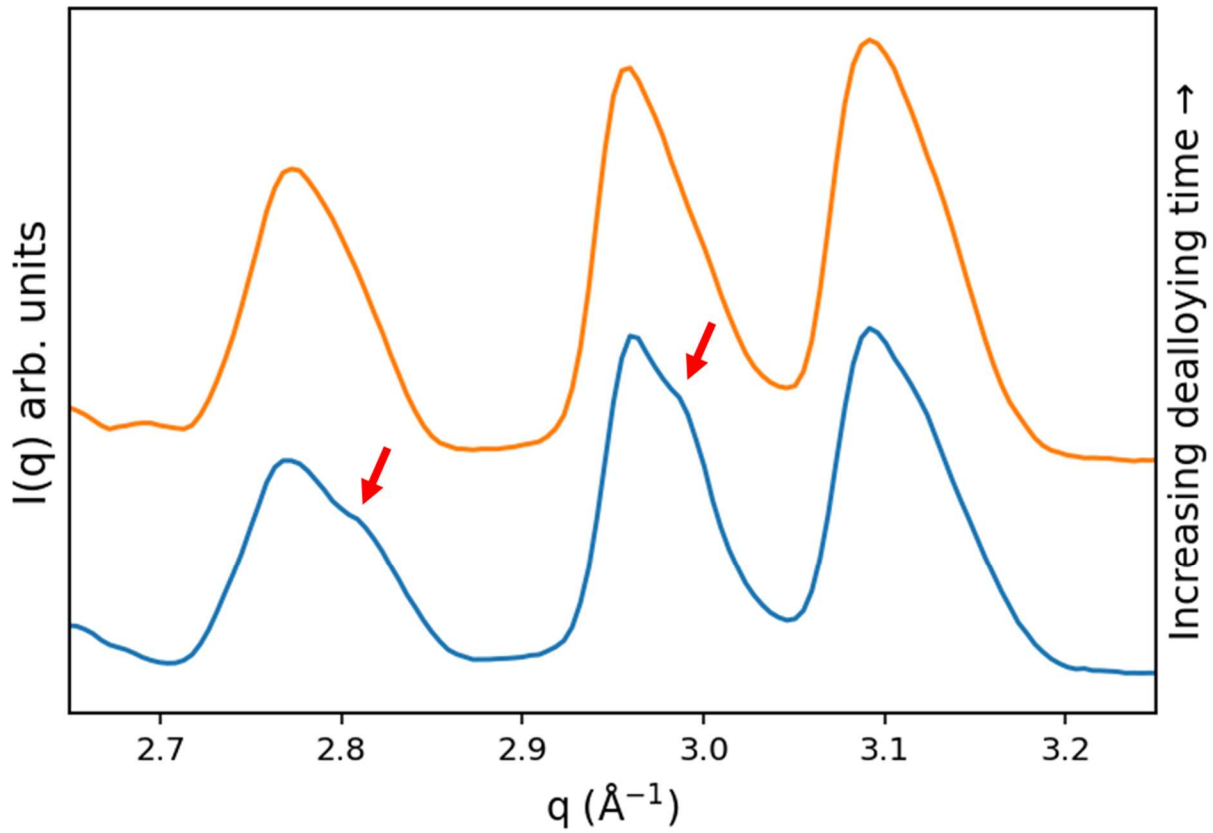

Figure 3.2 Scattering patterns for 30-70 parent alloy composition acquired at 0.3° incident angle after dealloying at 460° C for 7.5 minutes (blue) and 30 minutes (orange). Red arrows indicate locations of peak shoulders on the 7.5 minute spectra which may correspond to TiCu intermetallic formed before dealloying completion. Other peaks shown were determined to correspond to the same $CuMg_2$ and Cu_2Mg phases identified in Figure 3.1.

3.3 Multiparameter Data Visualization

Exploring a multiparameter space, such as an SSID dealloying system, can be made more efficient by visualizing the variation of multiple parameters at the same time. In the case of GIWAXS data this was achieved by mapping the intensity of a particular phase as a function of two system parameters. For instance, in Figure 3.3 characteristic peaks for Ti, $CuMg_2$, and Cu_2Mg phases are mapped as a function of the parent alloy composition as well as the measured incident angle (theta) on samples dealloyed at 460 °C for 30min. Note for this analysis Ti-Cu 50-50 parent alloy

composition is excluded due to sample breaking. By varying theta, we can observe how the intensity of any particular phase changes at different depths into the thin film sample. For this analysis peak areas were calculated using an in-house Python script which utilizes SciPy's *signal* module to determine which peak in each GIWAXS pattern is located closest to the known reference peak location. The script then integrates over this peak, using the full width half maximum (FWHM) to determine the bounds of integration as well as the integral baseline. For weak signals such as the Ti (110) phase peak this methodology was problematic since occasionally there would be no peak at the reference location, so a random nearby peak would be selected instead. To mitigate this issue, for the Ti phase a manual region of interest (ROI) was added to the script, and if the peak nearest to the reference location was outside the ROI the area would be automatically set to zero.

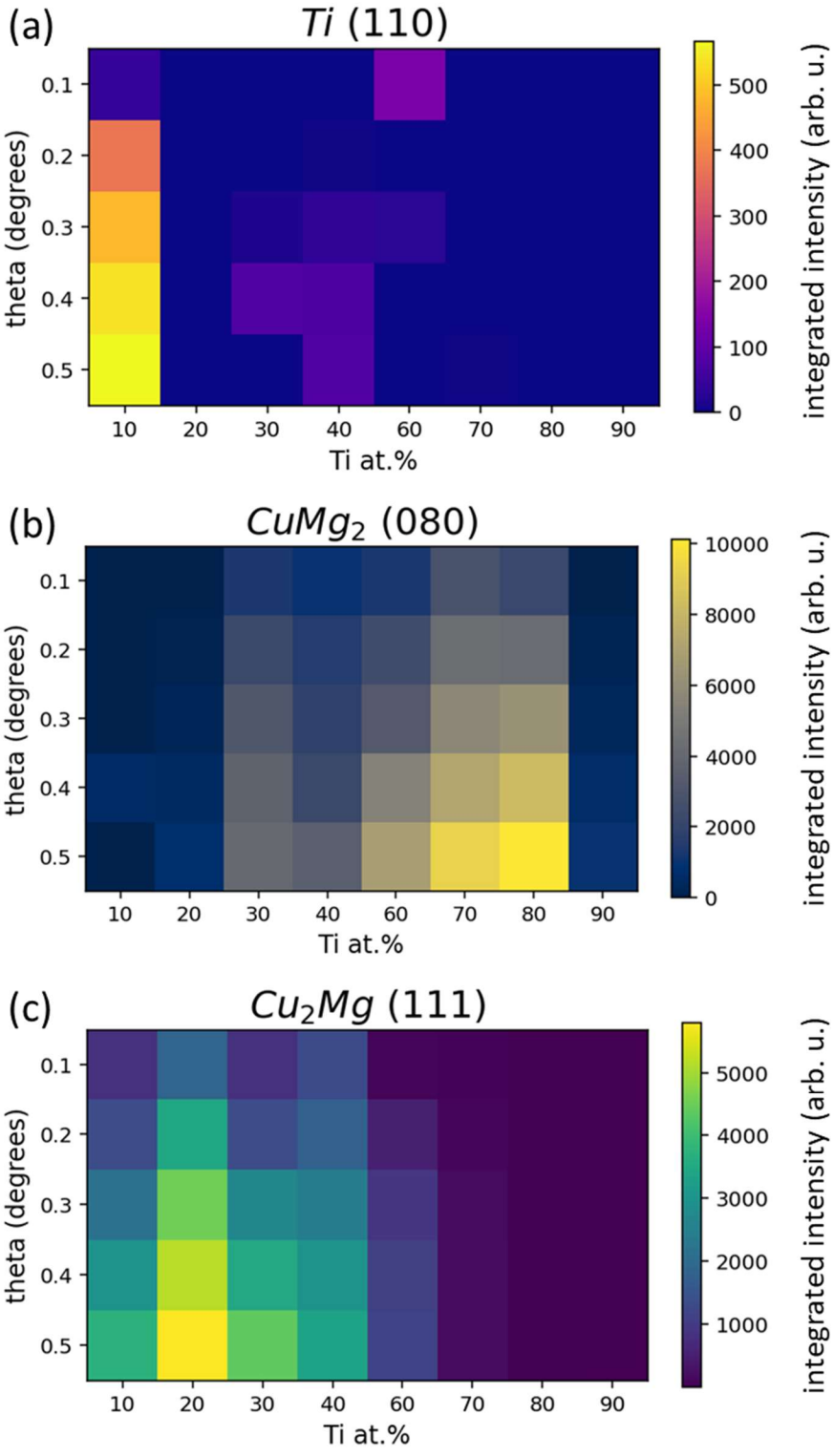

Figure 3.3 Quantification of phases by XRD peak intensity mapping for Ti (a), $CuMg_2$ (b), and Cu_2Mg (c) phases as a function of parent alloy composition and measurement incident angle (theta). Note that 50 at.% Ti parent alloy composition is excluded due to sample breaking.

Figure 3.3 shows that each selected phase has increasing intensity with increasing theta. This suggests that even at the greatest theta of 0.5° these measurements did not reach the critical angle at which the bottom parent alloy layer of the thin films is probed more than the top solvent layer. This is because beyond the critical angle we would expect to see a significant decrease in Cu-Mg intermetallic phase signals along with increased Ti signal. Moreover Figure 3.3 allows us to see the $CuMg_2$ and Cu_2Mg phases propagate a similar amount into the solvent top layer after dealloying, and the phase transition from $CuMg_2$ to Cu_2Mg at greater parent alloy Cu at.% can again be seen in comparing Figure 3.3(b) to Figure 3.3(c). At first inspection the results for the Ti phase mapping in Figure 3.3(a) may seem strange, since the most intense region of the map by far is at the lowest Ti at. %. However, taking a closer look at the Ti (110) peak in the actual scattering patterns reveals that this peak is often overshadowed by the much more prominent nearby $CuMg_2$ (080) peak, except for the Ti-Cu 10-90 sample since at this composition there is no $CuMg_2$ signal due to the phase transition into Cu_2Mg. This effect can be seen at theta of 0.3° in Figure 3.4. Figure 3.4 also highlights that in general the Ti phase signal was much weaker than that of other phases such as the Cu-Mg intermetallics, possibly due to critical angle not being reach during experimental measurement. Overall, this example demonstrates the importance of using multiple techniques to visualize multiparameter datasets especially when considering anomalous results from a particular visualization technique.

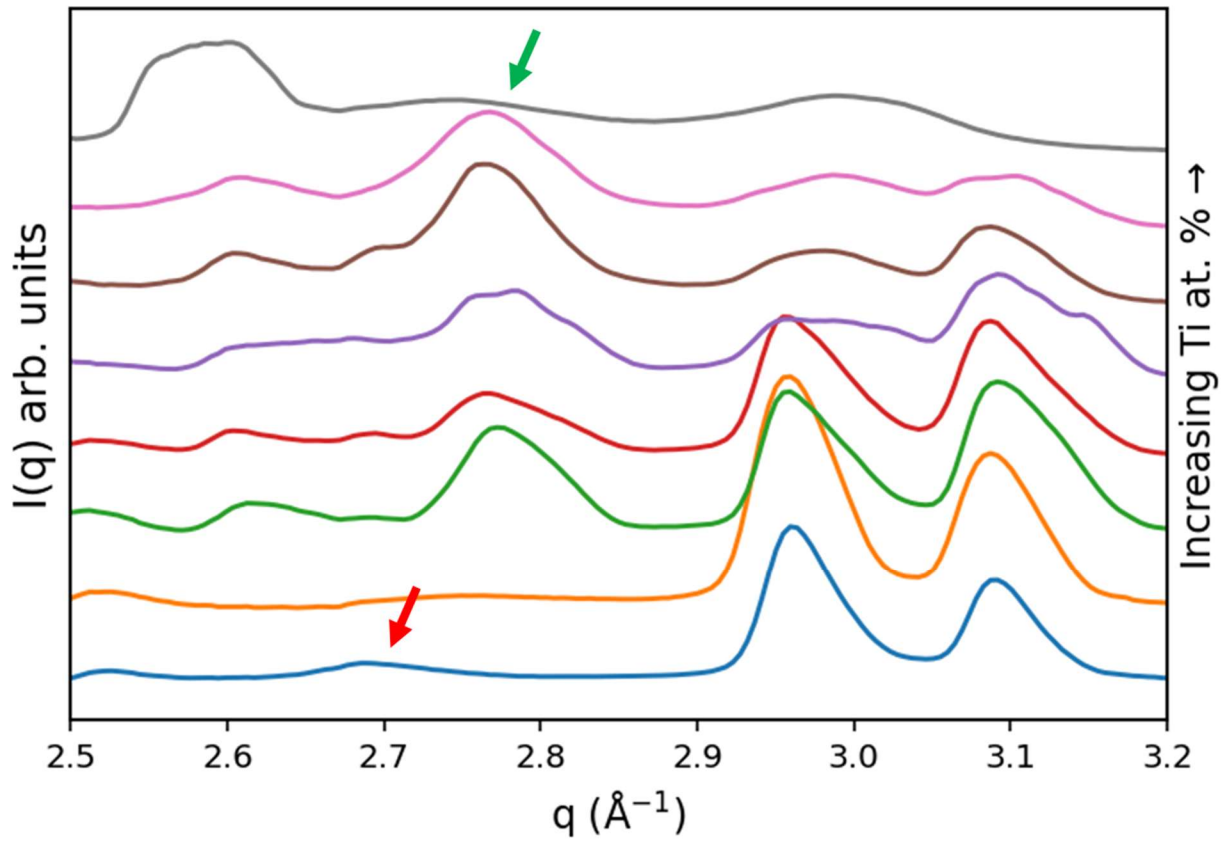

Figure 3.4 Plot of selected portion of GIWAXS patterns to highlight relative weakness of Ti (110) peak signal, indicated with bottom red arrow, and overshadowing by nearby $CuMg_2$ (080) peak signal, indicated with top green arrow. Patterns are shown for varying parent alloy compositions 10 at.% Ti to 90 at.% Ti with 10 at.% increment. Note 50 at.% Ti is excluded due to sample breaking.

3.4 Future Analysis

Altogether this analysis demonstrates some of the multiparameter data visualization capabilities of standard Python data science packages such as Matplotlib and SciPy, as well as the benefit of incorporating more specialized packages such as PeakUtils. By developing programmatic data visualization tools using these packages, future analysis can be faster and more streamlined. For example, future analysis could apply the same parameterization and visualization techniques to a GIWAXS dataset on dealloyed samples after chemical etching to gain more information about the

Ti phase evolution. Likewise, using the same analysis tools the effect of varying processing parameters such as dealloying time and temperature can be further explored.

Chapter 4. Conclusion

Altogether this work showed the implementation of a range of data science techniques to three separate studies of functional materials using synchrotron X-ray data analysis. In the first case, the tools of linear algebra were applied to XAS analysis by first understanding how an XAS dataset can be thought of in terms of vectors and matrices. Then using the specialized pyMCR package an MCR-ALS algorithm was applied for spectral decomposition. This analysis also relied on the XView package developed at the ISS beamline of NSLS-II. This highlights the importance of each level of software development for advanced data analysis. For instance, the pyMCR package handled the mathematics of spectral decomposition, the GUI of XView was critical in streamlining the user interface so that many different initial guesses for the pure components could be tested.

In the second example, a combination of open-source packages such as scikit-image and OpenCV were used in conjunction with Avizo commercial software for 3D nanotomography analysis. Moreover, the analysis of in-situ X-ray nanotomography data shows the need to think multidimensionally for synchrotron science, in this case dealing with both spatial and time-resolved data. Likewise, the final chapter also showed the need to think multidimensionally, but for the purposes of exploring multiparameter spaces such as the various processing parameters that characterize thin film SSID.

Many in the synchrotron community have already recognized the crucial role of data acquisition, management, analysis, and visualization for the future of synchrotron science [27]. This can be seen in the development of robust data pipelines and tools such as Brookhaven National Laboratory's Bluesky framework, which facilitates the use of scientific Python packages

throughout the experimental process, or in the development of open-source software such as the Tomviz package by Kitware Inc., which provides streamlined tools for tomography data analysis and visualization [1, 28]. However, this work has shown the amount opportunity available on the user-side to develop custom pipelines that streamline or automate specific tasks for each project. As the field of synchrotron research continues to advance, the role of data science in extracting valuable insights from experimental data is becoming increasingly important. User-created pipelines at synchrotron facilities will continue to rely on a diverse range of software packages, both commercial and open-source. However, the key to unlocking the full potential of synchrotron data lies in mastering the data science tools and techniques necessary to process and visualize complex, multidimensional data. As we move into the future, the trend towards greater integration of data science into synchrotron research is only set to continue. With the ability to efficiently analyze and interpret vast amounts of data, scientists will be able to uncover new insights and push the boundaries of what is possible in synchrotron research.

References

1. Chen-Wiegart, Y.-C.K., et al., *Multimodal Synchrotron Approach: Research Needs and Scientific Vision*. 2020, Taylor & Francis.
2. Martini, A. and E. Borfecchia, *Spectral decomposition of X-ray absorption spectroscopy datasets: methods and applications.* Crystals, 2020. **10**(8): p. 664.
3. Calvin, S., *XAFS for Everyone*. 2013: CRC press.
4. Ravel, B. *ATHENA: XAS Data Processing*. 2016; Available from: http://bruceravel.github.io/demeter/documents/Athena/index.html.
5. Zimmermann, P., et al., *Modern X-ray spectroscopy: XAS and XES in the laboratory.* Coordination Chemistry Reviews, 2020. **423**: p. 213466.
6. Camp, C.H., *pyMCR: A Python Library for Multivariate Curve Resolution Analysis with Alternating Regression (MCR-AR).* Journal of Research of the National Institute of Standards and Technology, 2019. **124**.
7. Henry, E.R. and J. Hofrichter, *Singular Value Decomposition - Application to Analysis of Experimental-Data.* Methods in Enzymology, 1992. **210**: p. 129-192.
8. Olivieri, A.C., *A down-to-earth analyst view of rotational ambiguity in second-order calibration with multivariate curve resolution − a tutorial.* Analytica Chimica Acta, 2021. **1156**: p. 338206.
9. Leshchev, D., *ISS factor analysis tools*. 2022.
10. Mathew, K., et al., *High-throughput computational X-ray absorption spectroscopy.* Scientific Data, 2018. **5**.
11. Chen, Y.M., et al., *Database of ab initio L-edge X-ray absorption near edge structure.* Scientific Data, 2021. **8**(1).
12. Jain, A., et al., *Commentary: The Materials Project: A materials genome approach to accelerating materials innovation.* Apl Materials, 2013. **1**(1).
13. Liu, X.Y., et al., *Formation of three-dimensional bicontinuous structures via molten salt dealloying studied in real-time by in situ synchrotron X-ray nano-tomography.* Nature Communications, 2021. **12**(1).
14. Ghaznavi, T., et al., *Alloying effects in high temperature molten salt corrosion.* Corrosion Science, 2022. **197**.
15. Guo, S.Q., et al., *Corrosion in the molten fluoride and chloride salts and materials development for nuclear applications.* Progress in Materials Science, 2018. **97**: p. 448-487.
16. Badwe, N., et al., *Decoupling the role of stress and corrosion in the intergranular cracking of noble-metal alloys.* Nature materials, 2018. **17**(10): p. 887-893.
17. Bell, S., T. Steinberg, and G. Will, *Corrosion mechanisms in molten salt thermal energy storage for concentrating solar power.* Renewable & Sustainable Energy Reviews, 2019. **114**.
18. Ding, W.J., A. Bonk, and T. Bauer, *Corrosion behavior of metallic alloys in molten chloride salts for thermal energy storage in concentrated solar power plants: A review.* Frontiers of Chemical Science and Engineering, 2018. **12**(3): p. 564-576.
19. Lee, W.-K. *Full Field X-ray Imaging*. National Synchrotron Light Source II Beamlines; Available from: https://www.bnl.gov/nsls2/beamlines/beamline.php?r=18-ID.
20. Bawane, K., et al., *Visualizing time-dependent microstructural and chemical evolution during molten salt corrosion of Ni-20Cr model alloy using correlative quasi in situ TEM and in situ synchrotron X-ray nano-tomography.* Corrosion Science, 2022. **195**: p. 109962.
21. Ge, M. and W.-K. Lee, *PyXAS–an open-source package for 2D X-ray near-edge spectroscopy analysis.* Journal of Synchrotron Radiation, 2020. **27**(2): p. 567-575.
22. Van der Walt, S., et al., *scikit-image: image processing in Python.* PeerJ, 2014. **2**: p. e453.
23. Bradski, G. and A. Kaehler, *OpenCV.* Dr. Dobb's journal of software tools, 2000. **3**: p. 120.
24. Zhao, C., et al., *Kinetics and Evolution of Solid-State Metal Dealloying in Thin Films with Multimodal Analysis.* Acta Materialia, 2022: p. 118433.

25. Zhao, C., et al., *Design nanoporous metal thin films via solid state interfacial dealloying.* Nanoscale, 2021. **13**(42): p. 17725-17736.
26. Negri, L.H., *PeatUtils*. 2021.
27. Hill, J., et al., *Future trends in synchrotron science at NSLS-II.* Journal of Physics: Condensed Matter, 2020. **32**(37): p. 374008.
28. Allan, D., et al., *Bluesky's Ahead: A Multi-Facility Collaboration for an a la Carte Software Project for Data Acquisition and Management.* Synchrotron Radiation News, 2019. **32**(3): p. 19-22.